

A forward-imaging needle-type OCT probe for image guided stereotactic procedures

Chia-Pin Liang,¹ Jeremiah Wierwille,¹ Thais Moreira,^{2,3} Gary Schwartzbauer,⁴
M. Samir Jafri,^{2,3} Cha-Min Tang,^{2,3} and Yu Chen^{1,*}

¹Fischell Department of Bioengineering, University of Maryland, College Park, MD 20742 USA

²Department of Neurology, University of Maryland School of Medicine, Baltimore, MD 21201 USA

³Research Service, Baltimore VA Medical Center, Baltimore, MD 21201 USA

⁴Department of Neurosurgery, University of Maryland School of Medicine, Baltimore, MD 21201 USA

*yuchen@umd.edu

Abstract: A forward-imaging needle-type optical coherence tomography (OCT) probe with Doppler OCT (DOCT) capability has the potential to solve critical challenges in interventional procedures. A case in point is stereotactic neurosurgery where probes are advanced into the brain based on predetermined coordinates. Laceration of blood vessels in front of the advancing probe is an unavoidable complication with current methods. Moreover, cerebrospinal fluid (CSF) leakage during surgery can shift the brain rendering the predetermined coordinates unreliable. In order to address these challenges, we developed a forward-imaging OCT probe (740 μm O.D.) using a gradient-index (GRIN) rod lens that can provide real-time imaging feedback for avoiding at-risk vessels (8 frames/s with 1024 A-scans per frame for OCT/DOCT dual imaging) and guiding the instrument to specific targets with 12 μm axial resolution (100 frames/s with 160 A-scans per frame for OCT imaging only). The high signal-to-background characteristic of DOCT provides exceptional sensitivity in detecting and quantifying the blood flow within the sheep brain parenchyma in real time. The OCT/DOCT dual imaging also demonstrated its capability to differentiate the vessel type (artery/vein) on rat's femoral vessels. We also demonstrated in *ex vivo* human brain that the location of the tip of the OCT probe can be inferred from micro-anatomical landmarks in OCT images. These findings demonstrate the suitability of OCT guidance during stereotactic procedures in the brain and its potential for reducing the risk of cerebral hemorrhage.

©2011 Optical Society of America

OCIS codes: (170.4500) Optical coherence tomography; (170.3880) Medical and biological imaging; (170.2150) Endoscopic imaging; (110.2760) Gradient-index lenses.

References and Links

1. H. J. Colbassani, S. Nishio, K. M. Sweeney, R. A. E. Bakay, and Y. Takei, "CT-assisted stereotactic brain biopsy: value of intraoperative frozen section diagnosis," *J. Neurol. Neurosurg. Psychiatry* **51**(3), 332–341 (1988).
2. N. K. Venkataramana, S. K. V. Kumar, S. Balaraju, R. C. Radhakrishnan, A. Bansal, A. Dixit, D. K. Rao, M. Das, M. Jan, P. K. Gupta, and S. M. Totev, "Open-labeled study of unilateral autologous bone-marrow-derived mesenchymal stem cell transplantation in Parkinson's disease," *Transl. Res.* **155**(2), 62–70 (2010).
3. A. E. Lang, S. Gill, N. K. Patel, A. Lozano, J. G. Nutt, R. Penn, D. J. Brooks, G. Hotton, E. Moro, P. Heywood, M. A. Brodsky, K. Burchiel, P. Kelly, A. Dalvi, B. Scott, M. Stacy, D. Turner, V. G. F. Wooten, W. J. Elias, E. R. Laws, V. Dhawan, A. J. Stoessl, J. Matcham, R. J. Coffey, and M. Traub, "Randomized controlled trial of intraputamenal glial cell line-derived neurotrophic factor infusion in Parkinson disease," *Ann. Neurol.* **59**(3), 459–466 (2006).
4. P. Limousin, P. Krack, P. Pollak, A. Benazzouz, C. Ardouin, D. Hoffmann, and A. L. Benabid, "Electrical stimulation of the subthalamic nucleus in advanced Parkinson's disease," *N. Engl. J. Med.* **339**(16), 1105–1111 (1998).

5. P. A. Starr, "Placement of deep brain stimulators into the subthalamic nucleus or Globus pallidus internus: technical approach," *Stereotact. Funct. Neurosurg.* **79**(3-4), 118–145 (2002).
6. P. D. Sawin, P. W. Hitchon, K. A. Follett, and J. C. Torner, "Computed imaging-assisted stereotactic brain biopsy: a risk analysis of 225 consecutive cases," *Surg. Neurol.* **49**(6), 640–649 (1998).
7. D. K. Binder, G. Rau, and P. A. Starr, "Hemorrhagic complications of microelectrode-guided deep brain stimulation," *Stereotact. Funct. Neurosurg.* **80**(1-4), 28–31 (2003).
8. D. K. Binder, G. M. Rau, and P. A. Starr, "Risk factors for hemorrhage during microelectrode-guided deep brain stimulator implantation for movement disorders," *Neurosurgery* **56**(4), 722–732, discussion 722–732 (2005).
9. M. I. Hariz, "Complications of deep brain stimulation surgery," *Mov. Disord.* **17**(S3 Suppl 3), S162–S166 (2002).
10. S. A. Boppart, B. E. Bouma, C. Pitriss, G. J. Tearney, J. G. Fujimoto, and M. E. Brezinski, "Forward-imaging instruments for optical coherence tomography," *Opt. Lett.* **22**(21), 1618–1620 (1997).
11. A. Sergeev, V. Gelikonov, G. Gelikonov, F. Feldchtein, R. Kuranov, N. Gladkova, N. Shakhova, L. Snopova, A. Shakhov, I. Kuznetzova, A. Denisenko, V. Pochinko, Y. Chumakov, and O. Streletzova, "*In vivo* endoscopic OCT imaging of precancer and cancer states of human mucosa," *Opt. Express* **1**(13), 432–440 (1997).
12. Y. Pan, H. Xie, and G. K. Fedder, "Endoscopic optical coherence tomography based on a microelectromechanical mirror," *Opt. Lett.* **26**(24), 1966–1968 (2001).
13. Y. Pan, Z. Li, T. Xie, and C. R. Chu, "Hand-held arthroscopic optical coherence tomography for *in vivo* high-resolution imaging of articular cartilage," *J. Biomed. Opt.* **8**(4), 648–654 (2003).
14. T. Xie, H. Xie, G. K. Fedder, and Y. Pan, "Endoscopic optical coherence tomography with a modified microelectromechanical systems mirror for detection of bladder cancers," *Appl. Opt.* **42**(31), 6422–6426 (2003).
15. J. M. Zara, S. Yazdanfar, K. D. Rao, J. A. Izatt, and S. W. Smith, "Electrostatic micromachine scanning mirror for optical coherence tomography," *Opt. Lett.* **28**(8), 628–630 (2003).
16. A. Jain, A. Kopa, Y. T. Pan, G. K. Fedder, and H. K. Xie, "A two-axis electrothermal micromirror for endoscopic optical coherence tomography," *IEEE J. Sel. Top. Quantum Electron.* **10**(3), 636–642 (2004).
17. X. Liu, M. J. Cobb, Y. Chen, M. B. Kimmey, and X. Li, "Rapid-scanning forward-imaging miniature endoscope for real-time optical coherence tomography," *Opt. Lett.* **29**(15), 1763–1765 (2004).
18. M. J. Cobb, X. Liu, and X. Li, "Continuous focus tracking for real-time optical coherence tomography," *Opt. Lett.* **30**(13), 1680–1682 (2005).
19. Y. Wang, M. Bachman, G. P. Li, S. Guo, B. J. Wong, and Z. Chen, "Low-voltage polymer-based scanning cantilever for *in vivo* optical coherence tomography," *Opt. Lett.* **30**(1), 53–55 (2005).
20. J. M. Zara and P. E. Patterson, "Polyimide amplified piezoelectric scanning mirror for spectral domain optical coherence tomography," *Appl. Phys. Lett.* **89**(26), 263901 (2006).
21. Z. Wang, C. S. Lee, W. C. Waltzer, J. Liu, H. Xie, Z. Yuan, and Y. Pan, "*In vivo* bladder imaging with microelectromechanical-systems-based endoscopic spectral domain optical coherence tomography," *J. Biomed. Opt.* **12**(3), 034009 (2007).
22. N. R. Munce, A. Mariampillai, B. A. Standish, M. Pop, K. J. Anderson, G. Y. Liu, T. Luk, B. K. Courtney, G. A. Wright, I. A. Vitkin, and V. X. Yang, "Electrostatic forward-viewing scanning probe for Doppler optical coherence tomography using a dissipative polymer catheter," *Opt. Lett.* **33**(7), 657–659 (2008).
23. Y. Takahashi, Y. Watanabe, and M. Sato, "High speed spectral domain optical coherence tomography with forward and side-imaging probe," *Jpn. J. Appl. Phys.* **47**(8), 6540–6543 (2008).
24. A. D. Aguirre, J. Sawinski, S. W. Huang, C. Zhou, W. Denk, and J. G. Fujimoto, "High speed optical coherence microscopy with autofocus adjustment and a miniaturized endoscopic imaging probe," *Opt. Express* **18**(5), 4222–4239 (2010).
25. C. P. Fleming, K. J. Quan, and A. M. Rollins, "Toward guidance of epicardial cardiac radiofrequency ablation therapy using optical coherence tomography," *J. Biomed. Opt.* **15**(4), 041510 (2010).
26. M. S. Jafri, S. Farhang, R. S. Tang, N. Desai, P. S. Fishman, R. G. Rohwer, C. M. Tang, and J. M. Schmitt, "Optical coherence tomography in the diagnosis and treatment of neurological disorders," *J. Biomed. Opt.* **10**(5), 051603 (2005).
27. M. S. Jafri, R. Tang, and C. M. Tang, "Optical coherence tomography guided neurosurgical procedures in small rodents," *J. Neurosci. Methods* **176**(2), 85–95 (2009).
28. J. G. Wu, M. Conry, C. H. Gu, F. Wang, Z. Yaqoob, and C. H. Yang, "Paired-angle-rotation scanning optical coherence tomography forward-imaging probe," *Opt. Lett.* **31**(9), 1265–1267 (2006).
29. S. Han, M. V. Sarunic, J. Wu, M. Humayun, and C. Yang, "Handheld forward-imaging needle endoscope for ophthalmic optical coherence tomography inspection," *J. Biomed. Opt.* **13**(2), 020505 (2008).
30. T. Xie, G. Liu, K. Kreuter, S. Mahon, H. Colt, D. Mukai, G. M. Peavy, Z. Chen, and M. Brenner, "*In vivo* three-dimensional imaging of normal tissue and tumors in the rabbit pleural cavity using endoscopic swept source optical coherence tomography with thoracoscopic guidance," *J. Biomed. Opt.* **14**(6), 064045 (2009).
31. T. Xie, S. Guo, Z. Chen, D. Mukai, and M. Brenner, "GRIN lens rod based probe for endoscopic spectral domain optical coherence tomography with fast dynamic focus tracking," *Opt. Express* **14**(8), 3238–3246 (2006).
32. L. Yu, G. Liu, M. Rubinstein, A. Saidi, B. J. Wong, and Z. Chen, "Office-based dynamic imaging of vocal cords in awake patients with swept-source optical coherence tomography," *J. Biomed. Opt.* **14**(6), 064020 (2009).
33. S. G. Guo, L. F. Yu, A. Sepehr, J. Perez, J. P. Su, J. M. Ridgway, D. Vokes, B. J. F. Wong, and Z. P. Chen, "Gradient-index lens rod based probe for office-based optical coherence tomography of the human larynx," *J. Biomed. Opt.* **14**(1), 014017 (2009).

34. Q. Li, M. L. Onozato, P. M. Andrews, C. W. Chen, A. Paek, R. Naphas, S. A. Yuan, J. Jiang, A. Cable, and Y. Chen, "Automated quantification of microstructural dimensions of the human kidney using optical coherence tomography (OCT)," *Opt. Express* **17**(18), 16000–16016 (2009).
35. S. Yuan, Q. Li, J. Jiang, A. Cable, and Y. Chen, "Three-dimensional coregistered optical coherence tomography and line-scanning fluorescence laminar optical tomography," *Opt. Lett.* **34**(11), 1615–1617 (2009).
36. S. Yuan, C. A. Roney, J. Wierwille, C. W. Chen, B. Y. Xu, G. Griffiths, J. Jiang, H. Z. Ma, A. Cable, R. M. Summers, and Y. Chen, "Co-registered optical coherence tomography and fluorescence molecular imaging for simultaneous morphological and molecular imaging," *Phys. Med. Biol.* **55**(1), 191–206 (2010).
37. V. X. D. Yang, M. L. Gordon, B. Qi, J. Pekar, S. Lo, E. Seng-Yue, A. Mok, B. C. Wilson, and I. A. Vitkin, "High speed, wide velocity dynamic range Doppler optical coherence tomography (Part I): System design, signal processing, and performance," *Opt. Express* **11**(7), 794–809 (2003).
38. N. Burris, K. Schwartz, C. M. Tang, M. S. Jafri, J. Schmitt, M. H. Kwon, O. Toshinaga, J. Y. Gu, J. Brown, E. Brown, R. Pierson 3rd, and R. Poston, "Catheter-based infrared light scanner as a tool to assess conduit quality in coronary artery bypass surgery," *J. Thorac. Cardiovasc. Surg.* **133**(2), 419–427 (2007).
39. S. W. Jeon, M. A. Shure, K. B. Baker, D. Huang, A. M. Rollins, A. Chahlavi, and A. R. Rezai, "A feasibility study of optical coherence tomography for guiding deep brain probes," *J. Neurosci. Methods* **154**(1-2), 96–101 (2006).
40. D. Morofke, M. C. Kolios, I. A. Vitkin, and V. X. D. Yang, "Wide dynamic range detection of bidirectional flow in Doppler optical coherence tomography using a two-dimensional Kasai estimator," *Opt. Lett.* **32**(3), 253–255 (2007).
41. D. C. Adler, Y. Chen, R. Huber, J. Schmitt, J. Connolly, and J. G. Fujimoto, "Three-dimensional endomicroscopy using optical coherence tomography," *Nat. Photonics* **1**(12), 709–716 (2007).
42. T. Klein, W. Wieser, C. M. Eigenwillig, B. R. Biedermann, and R. Huber, "Megahertz OCT for ultrawide-field retinal imaging with a 1050 nm Fourier domain mode-locked laser," *Opt. Express* **19**(4), 3044–3062 (2011).
43. J. Ren, J. Wu, E. J. McDowell, and C. Yang, "Manual-scanning optical coherence tomography probe based on position tracking," *Opt. Lett.* **34**(21), 3400–3402 (2009).

1. Introduction

Stereotactic procedures that require insertion of needle-based instruments into the brain serve important roles in neurosurgery. These procedures are employed in a variety of medical conditions from biopsy of suspected tumors [1] to cell-based and gene therapy [2,3] to the placement of electrodes that are used for deep brain stimulation (DBS) [4,5]. A fundamental limitation of these stereotactic procedures is that they are blind procedures in that the operator does not have real-time feedback as to what lies immediately ahead of the advancing probe. This results in two potential problems. The numerous medium sized blood vessels which cannot be detected by CT and MRI are at risk of being lacerated by the advancing probe. Lacerated vessels in the brain can lead to stroke and death [6–9]. Secondly, the brain may shift during surgery because of CSF leakage so that the intended target is no longer positioned at the pre-operatively determined coordinates. Misplacement of electrodes by millimeters in the brain can seriously decrease the effectiveness of DBS [5]. These two problems could be solved if the surgeon were able to visualize in real-time what is in front of the probe. Here we describe the design and demonstrate the imaging capability of a novel OCT probe for stereotactic neurosurgery that allows identification of blood vessels and anatomic landmarks in front of the advancing probe.

An effective image guidance probe for stereotactic procedures in the brain needs to satisfy three criteria. It must have a thin needle-like geometry (O.D. < 1 mm), forward-imaging capability, and the ability to detect blood vessels. Numerous forward-imaging probes have been developed for OCT [10–25], but their distal-end designs (> 1 mm) are too large to fit into the thin guide catheter used for stereotactic brain surgery. Previous studies propose a thin needle-type side-viewing OCT probe as a means for image guidance in DBS [26]. The probe has demonstrated that its resolution (15 μm) and sensitivity are sufficient to discern micro-anatomical landmarks in *ex vivo* human brains [26]. An *in vivo* small rodent study has demonstrated that the ability of detecting these landmarks in real time can guide the delivery of therapeutic agents or dissection to specific deep brain targets [27]. The weakness of this approach is that it cannot provide information on at-risk vessels in front of the advancing probe. Another novel design using a paired-angle-rotation scanning (PARS) probe [28,29] achieves forward-imaging needle-based (O.D. = 820 μm) endoscopy by using two counter-

rotating gradient-index (GRIN) lenses. Yet another group developed an elegant forward-imaging probe by relaying the scanning beam using a long GRIN rod lens, while keeping the endoscope itself stationary. This design provides fast dynamic focus tracking, which can perform high quality non-contact *in vivo* 3D imaging [30]. This design provides fast dynamic focus tracking, which can perform high quality non-contact *in vivo* 3D imaging [30]. Two different dynamic ranges of GRIN rod lenses have been reported: 72 dB and 108 dB [31,32]. In order to optimize the dynamic range, 8-deg-beveled glass windows and antireflection coating were applied to reduce the reflection from the end surface [30]. Previously reported GRIN-rod-lens-based probes are primarily for laryngoscopy or laparoscopy applications with probe sizes ranging from 2.7 to 4.58 mm [30–33]. To our knowledge, Doppler capability of the probes with O.D. smaller than 1 mm has not yet been demonstrated. This may be due to the difficulty of actuating the optics in such limited space. The limitations of existing approaches for OCT-guided stereotactic brain procedures motivated us to develop a GRIN-rod-lens approach that can satisfy the thin forward-imaging, needle-type criteria and the optical Doppler imaging criteria.

In this study, we demonstrated that the GRIN-rod-lens design can be miniaturized to a needle-imaging probe (O.D. = 740 μm). High-speed (100 frames/s) and high-sensitivity (>90 dB) OCT imaging was achieved by using this needle probe. The stationary GRIN-rod-lens also provides high quality DOCT imaging with 41 dB velocity dynamic range (VDR) and $\pm 17 \mu\text{m}/\text{s}$ velocity resolution. The effectiveness and robustness of the system was demonstrated in studies of sheep brain *in vivo* and human brain *ex vivo*.

2. Materials and methods

2.1 OCT handheld needle imaging device

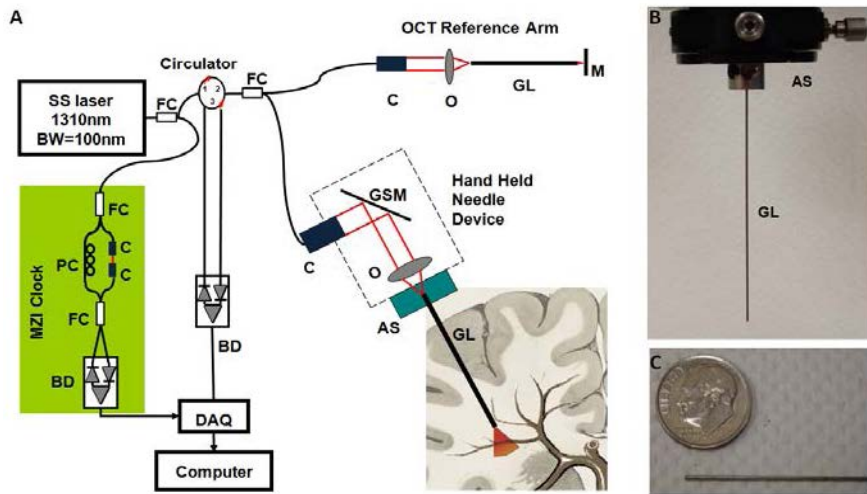


Fig. 1. (A) Schematic of the handheld OCT system. FC: fiber coupler; PC: polarization controller; C: collimator, BD: balanced detector, MZI: Mach-Zehnder interferometer (frequency clocks), DAQ: data acquisition board, M: mirror, GSM: galvanometer scanning mirror, O: objective lens, AS: alignment stages, GL: GRIN lens needle. (B) GRIN needle. (C) GRIN needle placed beside a U.S. dime.

Figure 1a shows the schematic of the OCT and handheld needle imaging device. The frequency domain OCT system [34–36] utilizes a wavelength-swept laser as its light source. Spectrum bandwidth of the laser is 100 nm centered at 1325 nm (Thorlabs, SL1325-P16). The wavelength-swept frequency is 16 kHz with 12 mW output power; therefore, for 160 axial lines images, the frame rate is equivalent to 100 frames per second. A Mach-Zehnder interferometer (MZI) receives 3% of the laser output power and uses it to generate a clock

signal with uniformly spaced optical frequency to trigger the sampling of the OCT signal in the analog-to-digital (A/D) converter. The sample and reference arms of a Michelson interferometer receives equal portions of the remaining 97% of the laser power. The galvanometer scanning mirrors deflect the sample arm light into the GRIN-rod imaging needle (NSG America, LRL-050-P400) through a low numerical aperture (NA) lens. Careful NA matching between GRIN lens (NA 0.084) and coupling lens ensures maximum coupling efficiency. The distal end of the GRIN needle receives the scanning laser spot from the proximal end and relays the backscattered signal back to the interferometer. The diameter of the GRIN lens is 0.5 mm and the outer diameter including the stainless steel tubing is 0.74 mm. To reduce the risk of blood vessel laceration and mechanical resistance in the tissue, we created a blunt tip by attaching a transparent cap to the distal end of the GRIN lens. Figure 1b shows the picture of the GRIN needle (GL) and Fig. 1c shows the GRIN needle placed beside a U.S. dime.

2.2 In vivo sheep brain deep vessel imaging

All procedures were approved by the Institutional Animal Care and Use Committee at the University of Maryland School of Medicine, and animals were treated in accordance with the PHS Policy on Humane Care and Use of Laboratory Animals, the National Institutes of Health Guide for the Care and Use of Laboratory Animals, and the Animal Welfare Act (7 U.S.C. et seq.). The effectiveness of the needle probe was evaluated by examining its ability to detect vessels below the surface of the parietal lobe of sheep ($n = 2$, male, wt. ~100 kg). Anesthesia was induced with 5 mg/kg ketamine (IV) and maintained under 1-4% isoflurane in 100% oxygen. After the sheep was deeply anesthetized, craniotomy was performed. The dura and pia membrane on the surface were carefully removed. Then, the imaging needle was inserted at the speed of 0.05 mm/s by a motorized stage. OCT and DOCT were acquired simultaneously at an imaging speed of 8 frames per second (1024 A-scans per frame) during the insertion. The velocity variance images were derived by a previously described method [37]. The variance signal is a surrogate of flow speed with a wider speed measurement range than DOCT signal and thus, less prone to alias problem existing in the DOCT images. Intensity threshold and a customized image segmentation algorithm were used to remove the noise in the variance images. The region of interest (ROI) is set in the area with high DOCT signal to noise ratio (SNR). A plot of the averaged variance signal in the ROI against time provides quantification of vessel pulsation. In one experiment, the OCT probe approached a vessel that was located within a deep sulcus and was held relatively immobile by the pia mater. In a second experiment, the OCT probe approached a vessel that was located within the brain parenchyma and could move with the brain tissue.

2.3 In vivo rat femoral vessel imaging

To demonstrate that the needle OCT device can differentiate artery from vein, we imaged the femoral vessels of Sprague-Dawley rats ($n = 4$, male, wt. ~400 g). Anesthetized rats (ketamine 50 mg/kg and xylazine 5 mg/kg, intraperitoneal) in supine position had their femoral vessels exposed and placed directly under the needle OCT probe. The blood vessel color and relative position to the femoral nerve allow visual identification of the artery and vein. The imaging speed of the simultaneously acquired OCT and DOCT images was 8 frames per second.

2.4 Ex vivo human brain imaging

To demonstrate the capability of this needle OCT device to image highly-scattering biological tissues and to determine the feasibility of using anatomic landmarks for locating the position of the imaging probe, we chose to image the human basal ganglia *ex vivo*. The basal ganglia is an appropriate region for this demonstration because it is the target of DBS for movement disorders [5] and because it contains high contrast structures that help in defining the

anatomic location. An unfixed coronal section containing the basal ganglia was placed on a motorized stage and kept moist by phosphate-buffered saline (PBS). The OCT probe was gradually inserted into the brain tissues by movement of the stage at a constant speed of 0.45 mm/s. OCT images were recorded along with the needle insertion at 100 frames/s (160 A-scans per frame). We also reconstructed full-track OCT images for correlating OCT landmarks with brain structures. The reconstructed OCT images were formed by splicing sub-regions from raw OCT images. A band of pixels (0.44 mm width, 0.0045 mm length) located at 0.2 mm from the distal surface of the GRIN lens was excised from each raw OCT images and rejoined to form the reconstructed image along the track of insertion passage.

3. Results

3.1 Characterization of forward imaging OCT needle

The forward-imaging needle probe can resolve microstructure with great sensitivity as shown by imaging of a lemon (Fig. 2a). The major barrier to optimize the sensitivity is the high reflection from both surfaces of the GRIN rod lens. We tackled this problem by attaching a high refractive index cap ($n = 1.56$, which is close to the refractive index of GRIN lens $n = 1.61$) at the distal end, and using oblique illumination at the proximal end to minimize specular reflection. The sensitivity was quantified by measuring the attenuated reflection from a high reflector (mirror). The attenuation from the neutral density filter is 36 dB and the mirror reflection is 54 dB. Therefore, our sensitivity is 90 dB. With careful dispersion matching at the reference arm by another GRIN-rod lens (with the same specification as the one used in the sample arm), the axial resolution was optimized. We characterized the axial resolution by measuring a reflective mirror (Fig. 2b). The axial resolution defined by the full width half maximum (FWHM) of the reflection surface is 17 μm in air (or 12 μm in tissue assuming an index of refraction of 1.4). The transverse resolution was measured by scanning a laser spot across a sharp edge of a reflective metal line on a US Air Force target (Fig. 2c). The distance between 10 and 90% intensity is 13 μm . The field-of-view (FOV) is limited by the diameter of GRIN rod lens. For a 0.5 mm diameter GRIN lens, the FOV is 0.44 mm.

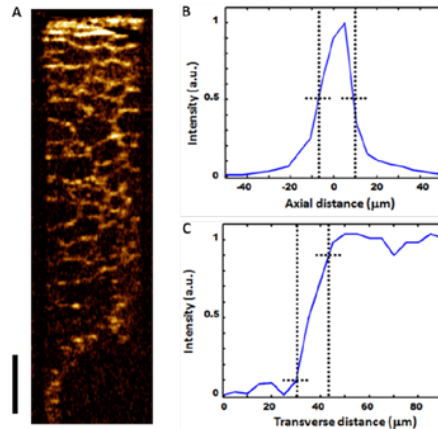


Fig. 2. (A) An OCT image of lemon acquired by a forward-imaging OCT probe. The scale bar is 0.25 mm. (B) The axial intensity plot of a highly reflective mirror. The axial resolution determined by FWHM is 17 μm in air (or 12 μm in tissue). (C) The intensity plot across a sharp edge on a US Air Force target. The transverse resolution determined by 10-90% positions is 13 μm .

3.2 In vivo sheep brain deep vessel imaging

The blood vessel DOCT imaging from an anesthetized sheep by the needle probe shows the feasibility of vessel detection *in vivo*. Figure 3 shows OCT and DOCT superimposed images

at different time points in the videos (Fig. 3 ([Media 1](#), [2](#), [3](#))) of a vessel as it was detected, monitored, and then compressed by the advancing probe. The OCT images in Fig. 3 ([Media 1](#), [2](#), [3](#)) shows that the speckle size in the lumen of vessels is much smaller than the speckle size of the wall making the boundary of the vessel wall easy to identify. The colormap scale for the DOCT signal is analogous to the colormap used for ultrasound Doppler signals. Red to yellow represents increasing flow speed in one direction whereas blue to cyan represents increasing speed in the opposite direction. However, the alias rings in these images do not indicate the change of flow direction. Instead, the abrupt change of color represents higher velocity that is “wrapped.” “Wrapping” occurs because the velocity exceeds the velocity dynamic range (VDR). When velocities exceed this limit in either direction, they “wrap” to values at the other end of colormap [37]. The superimposed image further verified the boundary of lumen and indicated that this system can provide measurement of the vessel size (~0.2 mm in diameter) that is verified by both OCT and DOCT. Figure 3a shows a vessel was detected in front of the probe. Figure 3 ([Media 1](#)) shows the probe was approaching the vessel. Figure 3b shows an image of the probe that was stopped right before hitting the vessel. Figure 3 ([Media 2](#)) shows the vessel pulsation while keeping the probe still. The periodic changes observed in the flow speed images strongly suggest that the vessel is a pulsating artery. Figure 3c shows the needle probe compressing the vessel. Figure 3 ([Media 3](#)) shows that, with the probe advancing gradually, the lumen of vessel becomes more and more constricted and the Doppler signal also decreases accordingly. Figure 4 shows that the pulsation can be quantified by flow velocity variance. Flow velocity variance varies monotonically with flow velocity and has a wider measurement range [36]. Therefore, it provides more accurate estimation of the flow speed than the aliased DOCT signal. However, it is prone to large error in regions with low SNR, so we set our ROI in a region having stable DOCT signal (the black rectangle in the variance image). Both DOCT and variance images show a dramatic difference between peaks and valleys. The larger red signal area in the DOCT images indicates higher flow velocity at the peaks. Also, the variance images show stronger signal corresponding to the higher flow velocity at peak. The average of the ROI variance signal versus time shows clear pulsation pattern. The heart rate is 80 beats per minutes. The high SNR Doppler signal enables us not only to detect the vessel but also to monitor the physiological change of the blood flow.

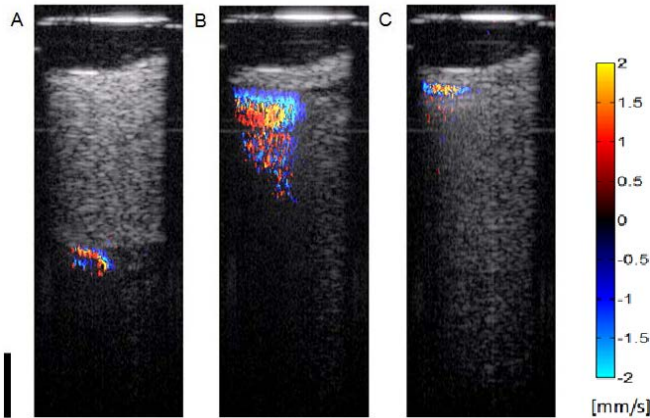


Fig. 3. Compression of a vessel by the OCT probe ([Media 1](#), [2](#), [3](#)). All the videos are from the same vessel. The bright line on the top of the images is the junction between GRIN rod lens and the transparent cap. The front curved surface of cap had direct contact with the tissue. The scale bar in all videos and the figure is 0.25 mm. (A) The OCT/DOCT superimposed image from [Media 1](#) shows a vessel 0.65 mm in front of the probe. (B) The superimposed image from [Media 2](#) shows a vessel right in front of the probe (C) The superimposed image from [Media 3](#) shows the vessel was compressed by the probe.

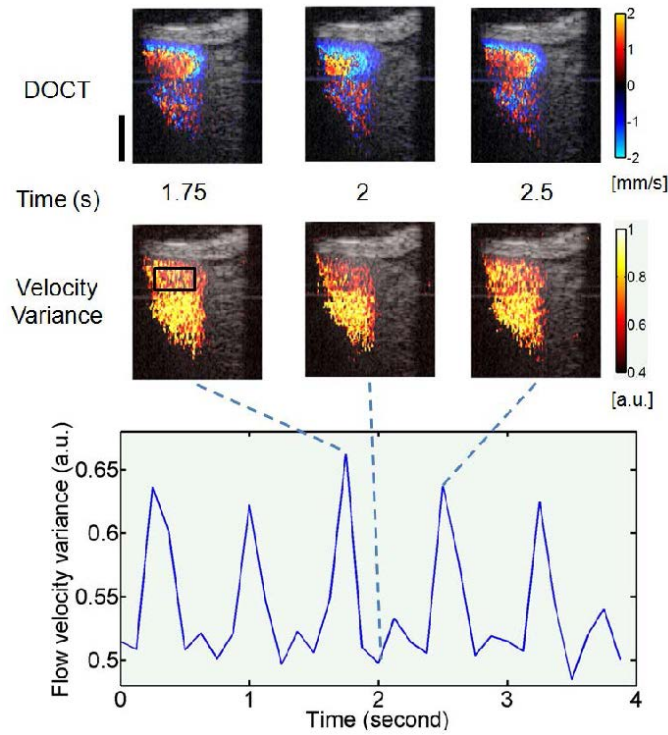


Fig. 4. The quantification of pulsation by flow velocity variance. The first row shows Doppler images at different time points specified in the second row. The third row shows the corresponding velocity variance images. The black rectangle shows the ROI. The value of flow velocity variance in the plot is the average value of ROI. The dashed lines indicate the time points of the corresponding image set. The scale bar is 0.2 mm.

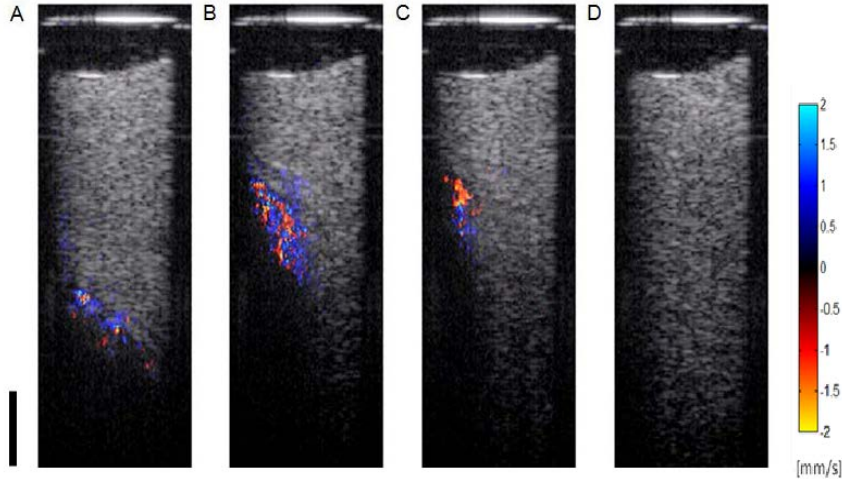


Fig. 5. Displacement of the blood vessel by the probe ([Media 4](#)). The images from A-D are in sequence as the probe was advancing. The scale bar in the video and the figure is 0.25 mm. The OCT/DOCT superimposed image of a vessel (A) 0.75 mm in front of the probe, (B) 0.35 mm in front of the probe with the vessel was being pushed aside, (C) 0.35 mm in front of the probe with the vessel was pushed further away from the probe, and (D) after the probe had passed the vessel.

An example of the vessel being pushed aside by the probe is shown in Fig. 5. A vessel was detected 0.93 mm in front of the probe by its Doppler signal (Fig. 5 ([Media 4](#))). As the probe approached to the vessel, the vessel is gradually pushed aside (Figs. 5a–5c) and finally out of the field of view (Fig. 5d). We also notice that the high blood flow speed in this large vessel made the Doppler alias rings smaller than the pixel size resulting in randomized Doppler signals. Although DOCT cannot provide quantitative flow data in this case, it still acts as a sensitive detection tool.

3.3 In vivo rat femoral vessel imaging

Imaging the rat femoral vessels shows the feasibility of vessel type differentiation by the OCT needle probe. The color and appearance of the rat femoral artery and vein distinguish them unequivocally by visual inspection. Figures 6a and 6b show both OCT and OCT/DOCT superimposed images of a rat femoral artery. Figures 6c and 6d are the images of the femoral vein. The bright lines at the top of images represent the end surface of the imaging needle. The speckle size and superimposed images allow us to differentiate the lumen and the vessel wall easily. The images show that the arterial wall is much thicker than the venous wall. Another distinguishing feature is the black outline surrounding the arterial lumen shown in Fig. 6a. This black outline is a muscular medial layer of endothelial lining lacking highly scattering elastin or collagen. In contrast, the medial layer in the vein typically contains more elastin and collagen [38]. Therefore, in Fig. 6c, we do not find this black layer. Furthermore, the steeper flow speed gradient in the artery leads to much denser alias rings in Doppler images (Fig. 6b vs. Fig. 6d). Therefore, the wall thickness, black inner lining and flow speed are three important parameters for differentiating the vessel types.

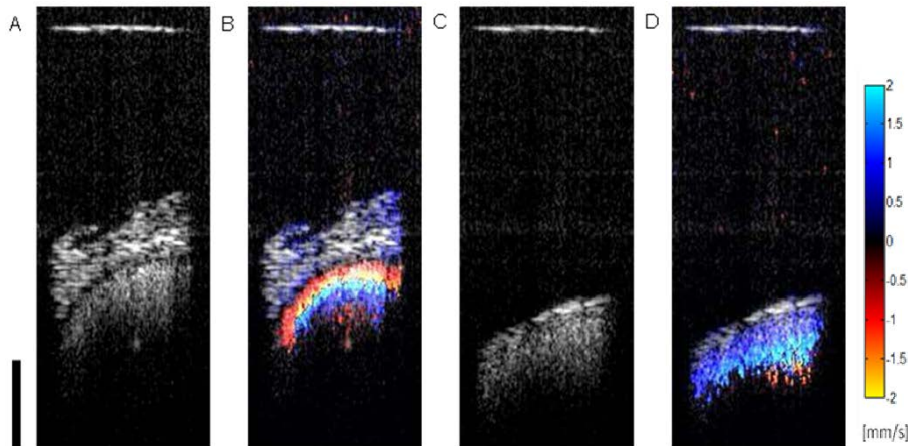


Fig. 6. OCT and OCT/DOCT superimposed images of rat femoral vessels. The scale bar represents 0.25 mm. (A) OCT image of femoral artery. (B) Superimposed image of femoral artery. (C) OCT image of femoral vein. (D) Superimposed image of femoral vein.

3.4 Ex vivo human brain imaging

The images of the human basal ganglia *ex vivo* illustrate the potential for neurosurgical guidance. Figure 7 shows a camera image of human brain tissue and the full-track reconstructed OCT image. In the camera image of brain tissue, note the white appearance of fiber tracts surrounding the gray matter nuclei and the striation of white fiber bundles within the putamen. The reconstructed OCT track was obtained by pushing the probe from right to left 2 mm below and parallel to the surface of the brain slice. This figure illustrates the high degree of contrast between gray and white matter generated by OCT. The transition between

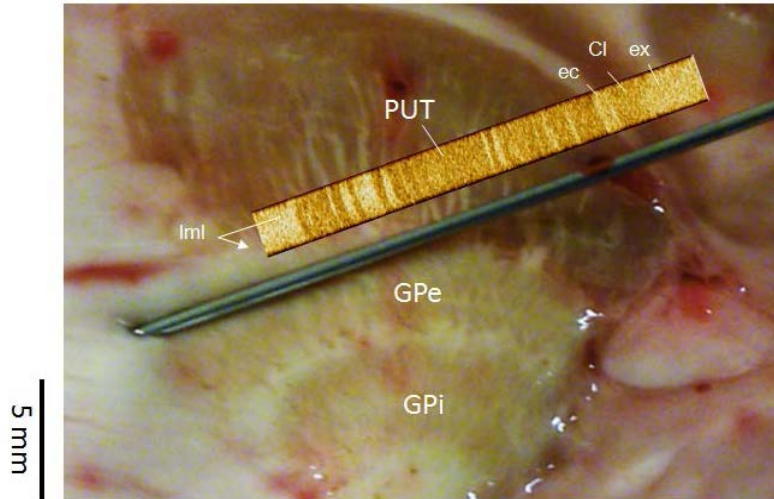


Fig. 7. A camera image of the needle-type OCT probe sitting on top of the human basal ganglia with the full-track reconstructed OCT image ([Media 5](#)). In [Media 5](#), the scale bar on the left represents 0.25 mm and the scale bar on the right represents 3 mm. The probe on top of the brain tissue shows relative dimension and the direction of insertion (from top right to bottom left). The full-track OCT image is placed proximal to the insertion passage. Major structures are labeled: extreme capsule (ex), claustrum (Cl), external capsule (ec), putamen (PUT), lateral medullary lamina (lml), globus pallidus externa (GPe) and globus pallidus interna (GPI). The width of the reconstructed OCT images in both [Media 5](#) and this figure are expanded for better visualization. The real width is 0.44 mm.

the thin white fiber capsule, the gray matter putamen, and the lamina to the GPe can be clearly identified. These OCT-detectable structures are useful anatomic landmarks that can be used in stereotactic surgery [26,27,39].

The video to the left of Fig. 7 ([Media 5](#)) shows the OCT images as they were being acquired. The dynamic reconstruction is shown on the right. The structures identified in this passage include: extreme capsule (ex), claustrum (Cl), external capsule (ec), putamen (PUT), lateral medullary lamina (lml). The raw OCT video shows the difference between gray and white matter. The white matter typically has much higher intensity with shallower penetration depth. Also, the characteristic white matter striations in the putamen display high contrast and can be easily identified. Because the needle was inserted 2 mm below and parallel to the surface of the brain slice, the number and the size of the fiber tracts in the camera image are different from the fiber tracks in OCT image. Reconstruction of the full-track OCT image allows better identification of the probe location. The dynamic reconstruction video demonstrates how this was constructed. Figure 7 ([Media 5](#)) shows that our system can provide real-time imaging feedback to track the tip location. This information can assist in the guidance of therapeutic tools to deep brain targets with micrometer precision.

4. Discussion

An image-guidance probe for stereotactic neurosurgery needs to address multiple challenges. The fundamental challenge is to provide information on what is in front of the probe in real time for a procedure that is otherwise blind. The primary clinical objective is to avoid lacerating blood vessels in front of the advancing probe. A secondary objective is to obtain information on the position of the probe tip relative to anatomic landmarks. This has to be accomplished with a thin needle-like geometry that will fit inside existing stereotactic apparatus.

The GRIN-rod-lens approach provides a solution to the multiple requirements for stereotactic neurosurgery. By using motion-free GRIN rod lenses as relay optics, the high

speed A-line scanning rate of the laser system can be fully exploited without compromising the needle size. This high speed forward-imaging capability allows us to promptly avoid the at-risk vessels (Fig. 3 ([Media 1](#))) and locate the tip position (Fig. 7 ([Media 5](#))). Moreover, stable and high speed A-line scanning is critical for optimizing the flow VDR [37]. Unstable and slow A-line scanning rates will degrade VDR and hinder vessel detection by DOCT. Our system not only detects vessels but also monitors the physiological changes of the blood flow (Fig. 3 ([Media 2](#))). Since there is no complex actuation at the distal end, this probe is one of the thinnest forward-imaging OCT probes. The diameter of the probe is a compromise between providing sufficient field of view and minimizing tissue injury. A GRIN lens diameter of 0.5 mm and field of view of 0.44 mm allows easy recognition of vessels, and the overall diameter of 0.74 mm is smaller than the inner diameter of existing stereotactic cannulae. Our current GRIN rod lens has a length of 12 cm. A portion of the rod lens (2.5 cm) is used for interfacing the rod lens with the scanning head. Therefore we can insert 9.5 cm deep inside the brain. The current probe length is more than adequate to reach all existing targets of DBS in the human. It can also be used for brain tumor biopsy, ventricle identification, etc. Also, the length could be further extended by splicing several pieces of GRIN rods together.

Evaluating the system in a living large mammalian brain provides correlates to the conditions of clinical stereotaxis. While useful information can be obtained from studies in phantoms, rodents and *ex vivo* human tissue, these substitute samples cannot provide adequate simulation of the live human brain surgery. There are no vessels in the rat brain that are comparable in size to those in the human brain. Large animal brain imaging *in vivo* also provided an opportunity to determine the extent of a potential problem for DOCT. The brain moves in conjunction with respiration and heartbeat. We found that this was problematic for imaging surface vessels, but not for intraparenchymal vessels. The surgeons can bypass surface vessels because they can directly visualize them. Once the probe entered the brain parenchyma, the movement problem is greatly decreased, possibly because the probe appears to stabilize the tissue directly in front of it. Additionally, vessels within the parenchyma can be easily pushed to the side by the probe (Fig. 5 ([Media 4](#))), whereas vessels in deep sulci (Fig. 3 ([Media 3](#))) that are tightly attached to the pia mater are not easily pushed aside by the probe. Vessels in sulci are really surface vessels that are buried by the cortical folds. This is consistent with anecdotal experience of neurosurgeons who meticulously avoid entering cortical sulci.

Besides detecting the vessels, the probe can also monitor the pulsation (Fig. 4) and differentiate the vessel type (Fig. 6). These capabilities could be valuable for screening the vessels posing high risk in neurosurgery. We acknowledge that the aliasing problem may hinder using DOCT signal to quantify blood flow; however, we can work around this problem by using velocity variance [37] or axial Kasai algorithm [40]. Also, the high speed Fourier domain mode locking laser should be able to increase the velocity detection limit from one to two orders [41,42].

In addition to detecting the at-risk vessels, this forward-imaging needle-type OCT probe can be an important complementary technology for current stereotaxic neurosurgery. Prior studies have demonstrated the ability of catheter-based OCT to provide information on the position of the probe relative to neighboring anatomic landmarks [26,27]. Although the forward-scanning probe does not provide as much field of view as with the rotating side-imaging approach [26], the needle probe can be used to provide real-time feedback on the degree to which the brain has shifted due to the surgery induced CSF leak. This is accomplished by establishing the probe tip relative to critical landmarks such as a prominent gray matter-white matter junction (Fig. 7 and [Media 5](#)). Since the stereotactic system provides the expected position, any deviation between the expected and actual location of a landmark provides the surgeon useful information on the degree to which the brain has shifted during surgery. Secondly, it can often provide optical signatures of specific anatomic structures (i.e.

the pencils of fibers in the putamen). The use of image guidance probes in conjunction with pre-operative MRI or CT images will give the surgeons greater confidence on the probe location. However, for diagnosis of other pathologies, a wider FOV may be desired. A possible way is to reconstruct a wider FOV image using manual scanning and optical tracking [43]. The next phase of this project will be to miniaturize the overall proximal size and integrate a functional imaging modality. Besides the application in stereotactic procedures, this device can potentially be applied to many other image-guided interventions and for the detection of blood flow involving difficult to reach structures.

5. Conclusion

The forward-imaging needle-type OCT probe is a promising complementary technology for current stereotactic neurosurgery. With real time OCT/DOCT forward imaging capability, it may be possible to avoid laceration of at-risk intraparenchymal vessels and infer probe location relative to OCT detectable landmarks. The device described here may be adapted to multiple intervention procedures in addition to stereotactic neurosurgery.

Acknowledgments

We thank Professor James Fujimoto from MIT and Professor Changhuei Yang from Caltech for insightful discussion, Dr. James Jiang from Thorlabs Inc. for technical assistance, and Dr. John Wu from UMMC for assistance in animal experiment. This work is supported in part by the University of Maryland Baltimore (UMB) and College Park (UMCP) Seed Grant Program, the Nano-Biotechnology Award of the State of Maryland, the Prevent Cancer Foundation, A. Ward Ford Memorial Research Grant, NIH R21EB012215-01A1, R21DK088066-01A1, and grants from the Veterans Administration (TM, MSJ, and CMT).